

1 **Variation in CO<sub>2</sub> and CH<sub>4</sub> Fluxes Among Land Cover Types in Heterogeneous Arctic Tundra**  
2 **in Northeastern Siberia**

3

4 Sari Juutinen<sup>1,2</sup>, Mika Aurela<sup>1</sup>, Juha-Pekka Tuovinen<sup>1</sup>, Viktor Ivakhov<sup>3</sup>, Maiju Linkosalmi<sup>1</sup>, Aleksi  
5 Räsänen<sup>4,5</sup>, Tarmo Virtanen<sup>4</sup>, Juha Mikola<sup>4,6</sup> Johanna Nyman<sup>1</sup>, Emmi Vähä<sup>1</sup>, Marina Loskutova<sup>7</sup>,  
6 Alexander Makshtas<sup>7</sup>, and Tuomas Laurila<sup>1</sup>

7

8 1) Finnish Meteorological Institute, Climate System Research, Erik Palménin aukio 1, 00560  
9 Helsinki, Finland

10 2) Department of Geographical and Historical Studies, University of Eastern Finland,  
11 Yliopistonkatu 2, FI-80100 Joensuu, Finland (P.O. Box 111, FI-80101 Joensuu, Finland)

12 3) Voeikov Main Geophysical Observatory, Ulitsa Karbysheva, 7, St Petersburg, 194021,  
13 Russia

14 4) Ecosystems and Environment Research Programme, University of Helsinki, Viikinkaari 1,  
15 00790 Helsinki, Finland

16 5) Natural Resources Institute Finland (Luke), Paavo Havaksen tie 3,  
17 90570 Oulu, Finland

18 6) Natural Resources Institute Finland (Luke), Latokartanonkaari 9,  
19 00790 Helsinki, Finland

20 7) Arctic and Antarctic Research Institute, Bering str., 38, St Petersburg, 199397, Russia

21

22  
23 Corresponding author Sari Juutinen, sari.juutinen@uef.fi

24

25

26

27 **Abstract**

28 Arctic tundra is facing unprecedented warming, resulting in shifts in the vegetation, thaw regimes,  
29 and potentially in the ecosystem-atmosphere exchange of carbon (C). However, the estimates of  
30 regional carbon dioxide (CO<sub>2</sub>) and methane (CH<sub>4</sub>) budgets are highly uncertain. We measured CO<sub>2</sub>  
31 and CH<sub>4</sub> fluxes, vegetation composition and leaf area index (LAI), thaw depth, and soil wetness in  
32 Tiksi (71° N, 128° E), a heterogeneous site located within the prostrate dwarf-shrub tundra zone in  
33 northeastern Siberia. Using the closed chamber method, we determined net ecosystem exchange  
34 (NEE) of CO<sub>2</sub>, dark ecosystem respiration (ER), ecosystem gross photosynthesis (Pg), and CH<sub>4</sub>  
35 fluxes during the growing season. We applied a previously developed high-spatial-resolution land-  
36 cover map over an area of 35.8 km<sup>2</sup> for spatial extrapolation. Among the land-cover types varying  
37 from barren to dwarf-shrub tundra and tundra wetlands, the NEE and Pg at the photosynthetically  
38 active photon flux density of 800 μmol m<sup>-2</sup> h<sup>-1</sup> (NEE<sub>800</sub> and Pg<sub>800</sub>) were greatest in the graminoid-  
39 dominated habitats, i.e., streamside meadow and fens, with NEE<sub>800</sub> and Pg<sub>800</sub> of up to -21 (uptake)  
40 and 28 mmol m<sup>-2</sup> h<sup>-1</sup>, respectively. Vascular LAI was a robust predictor of both NEE<sub>800</sub> and Pg<sub>800</sub>  
41 and, on a landscape scale, the fens were disproportionately important for the summertime CO<sub>2</sub>  
42 sequestration. Dry tundra, including the dwarf-shrub-dominated vegetation and barren, had smaller  
43 CO<sub>2</sub> exchange rates. The fens were the dominant source of CH<sub>4</sub>, while the dry mineral soil tundra  
44 consumed atmospheric CH<sub>4</sub>, which on a landscape scale amounted to -9 % of the total CH<sub>4</sub> balance.  
45 The largest seasonal mean CH<sub>4</sub> consumption rate of 0.02 mmol m<sup>-2</sup> h<sup>-1</sup> occurred in sand- and stone-  
46 covered barren. The high consumption rate agrees with the estimate based on the eddy covariance  
47 measurements at the same site. We acknowledge the uncertainty involved in spatial extrapolations  
48 due to a small number of replicates per land-cover type. This study highlights the need to  
49 distinguish different land-cover types including the dry tundra habitats to account for their different  
50 CO<sub>2</sub> and CH<sub>4</sub> flux patterns, especially the consumption of atmospheric CH<sub>4</sub>, when estimating tundra  
51 C exchange on a larger spatial scale.

52 **1 Introduction**

53 It is uncertain whether the Arctic tundra is a sink or a source of atmospheric carbon (C). The current  
54 estimates suggest a sink of 13–110 Tg C yr<sup>-1</sup>, but their uncertainty range crosses the zero balance  
55 (McGuire et al. 2012, Virkkala et al. 2020). Improving these estimates is vital, because the Arctic  
56 tundra covers a vast area of 7.6 million km<sup>2</sup> (Walker 2000) that is experiencing substantial warming  
57 (IPCC 2013, Chen et al. 2021). Warming can alter C exchange, and either amplify or mitigate  
58 climate change through ecosystem–atmosphere interactions. Some local-scale studies suggest that  
59 the Arctic tundra is shifting from a small sink to a source of C (Webb et al. 2016, Euskirchen et al.  
60 2017). It is likely that the climate change response of the ecosystem carbon dioxide (CO<sub>2</sub>) sink  
61 strength and methane (CH<sub>4</sub>) emissions, whether an increase or a decrease, depends on site-specific  
62 changes in thawing, wetness, temperature, and vegetation (McGuire et al. 2018). Dynamics of C  
63 exchange need to be quantified across the Arctic habitats to improve the upscaling of arctic CO<sub>2</sub> and  
64 CH<sub>4</sub> balances and to monitor how ecosystems respond to environmental changes.

65 The uncertainty in the arctic C balance estimates arises from the sparse and uneven  
66 observation network, which provides poor support for model-based spatial extrapolation (*cf.*  
67 McGuire et al. 2018, Virkkala et al. 2021, Kuhn et al. 2021). On a local scale, landscape  
68 heterogeneity and the related difficulty of mapping the spatial distribution of habitats and their C  
69 fluxes add to this uncertainty (McGuire et al. 2012, Treat et al. 2018, Saunois et al. 2020). In  
70 addition, year-to-year variations in seasonal features, particularly the timing of spring, summer  
71 temperatures, and snow depth have been found to cause substantial variation in the annual net CO<sub>2</sub>  
72 and CH<sub>4</sub> balances (Aurela et al. 2004, Humphreys and Lafleur 2011, Zhang et al. 2019). Fine-scale  
73 spatial heterogeneity in soil water saturation, thaw depth, vegetation characteristics, and soil organic  
74 content is typical of the tundra landscape (*e.g.*, Virtanen and Ek 2014, Mikola et al. 2018, Lara et al.  
75 2020). These factors control CO<sub>2</sub> and CH<sub>4</sub> exchange, and on an annual scale, tundra wetlands  
76 typically act as net CO<sub>2</sub> sinks while upland tundra areas have a close-to-neutral CO<sub>2</sub> balance (*e.g.*,

77 Marushchak et al. 2013, Virkkala et al. 2021). While tundra wetlands are substantial sources of  
78 CH<sub>4</sub>, dry tundra acts as a small sink or small source of atmospheric CH<sub>4</sub> (Bartlett and Harriss 1993,  
79 Kuhn et al. 2021).

80 Mineral soil tundra barrens, however, have been found to have high consumption rates  
81 of atmospheric CH<sub>4</sub> which is due to the high-affinity methane oxidizing bacteria (Emmerton et al.  
82 2014, Jørgensen et al. 2014, D'Imperio et al. 2017, Oh et al. 2020). These bacteria can utilize  
83 atmospheric CH<sub>4</sub> as energy source at low atmospheric concentrations, opposite to the low-affinity  
84 methane oxidizers that require higher CH<sub>4</sub> concentrations and occur in wetlands (e.g., Oh et al.  
85 2020). A modeling exercise that introduced the high-affinity methanotrophy for mineral-rich soils  
86 resulted in a doubling of the circumpolar soil CH<sub>4</sub> sink above 50° N compared to previous estimates  
87 (Oh et al. 2020) Thus, distinguishing dry and wet tundra with their moisture and vegetation  
88 characteristics is crucial when mapping C exchange within the tundra biome. Treat et al. (2018)  
89 tested spatial resolution requirements for such mapping on a landscape level and found that a 20-m  
90 pixel size captured the spatial variation in a reasonable manner, while a coarser resolution resulted  
91 in underestimation of both the landscape-scale CO<sub>2</sub> uptake and CH<sub>4</sub> emissions. In addition,  
92 understanding the spatial heterogeneity of ecosystem C exchange substantially improves analyses of  
93 eddy covariance (EC) measurements that, while in principle representing spatially integrated fluxes,  
94 may provide biased gas flux balances in a highly heterogeneous source/sink environment, as the  
95 spatial integration of EC involves non-uniform weighting of the surface elements that contribute to  
96 the measured flux (Tuovinen et al. 2019).

97 The aim of this study was to assess the spatial patterns and magnitudes of CO<sub>2</sub> and  
98 CH<sub>4</sub> fluxes within heterogenous prostrate dwarf-shrub tundra in Tiksi, located in northeastern  
99 Russia. Growing season fluxes of CO<sub>2</sub> (ecosystem net exchange, photosynthesis, and respiration)  
100 and CH<sub>4</sub> were determined using the chamber method to answer the questions: (i) what is the  
101 magnitude of these fluxes in different land-cover types and (ii) how do they depend on vegetation

102 characteristics and soil wetness? In addition, we extrapolated the plot-level measurements in space  
103 and compared them with the ecosystem-level data measured with the EC technique.

104

105 **2 Materials and Methods**

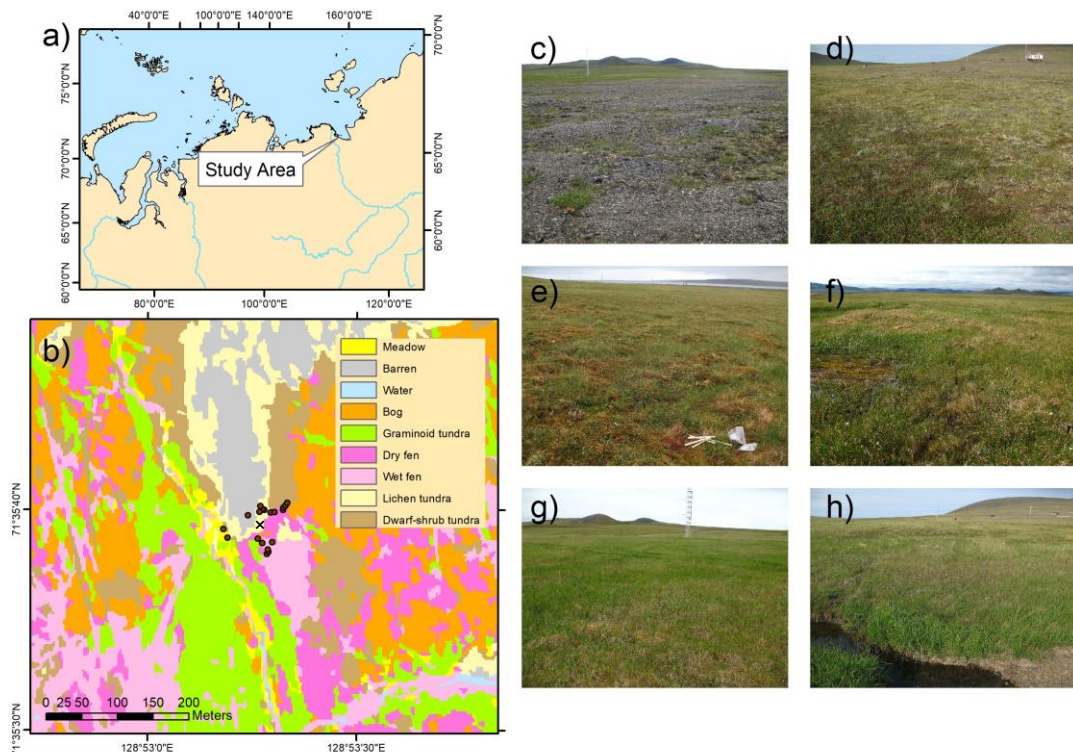
106 *2.1 Study site*

107 The study site is located near the Tiksi Observatory in Sakha (Yakutia) (see Uttal et al. 2016),  
108 northeastern Russia ( $71.5943^{\circ}$  N,  $128.8878^{\circ}$  E), 500 m inland off the Laptev Sea coast and, on  
109 average, 7 m above sea level (Fig. 1a). The area belongs to the middle-arctic prostrate dwarf-shrub  
110 tundra subzone (Walker, 2000) and has continuous permafrost. In the end of the growing season,  
111 the maximum thaw depth is *ca.* 40 cm (Mikola et al. 2018). The climate in Tiksi is defined by cold  
112 winters and cool summers. The long-term mean annual temperature and mean annual precipitation  
113 were  $-12.7^{\circ}\text{C}$  and 232 mm, respectively, during the climate normal period 1981–2010. Growing  
114 season lasts about 3 months, and the soils typically freeze in the end of September and the  
115 permanent snow falls in October and thaws in June (AARI 2018).

116 Bedrock is alkaline, resulting in high plant species richness. Vegetation consists of  
117 mosses, lichens, grasses, sedges, prostrate dwarf-shrubs such as willows (*Salix* spp.), dwarf birch  
118 (*Betula nana*), and *Diapensia lapponica*, and forb species (Table 1). The average heights of dwarf-  
119 shrub species are 4–6 cm and the leaf area index (LAI) of vascular plants reaches up to  $1\text{ m}^2\text{ m}^{-2}$  in  
120 the fen and meadow habitats with graminoid vegetation (Juutinen et al. 2017). The land cover at the  
121 site has been classified *a priori* and mapped based on a combination of field inventories and high-  
122 spatial resolution satellite images (Mikola et al. 2018). The *a priori* land-cover types (LCTs) consist  
123 of wet fen, dry fen, graminoid tundra, bog, meadow at the stream bank, dwarf-shrub tundra, and  
124 lichen tundra that consists of barren ground with rocks and sand and patches of vegetation (Table 1,  
125 Fig. 1 c–h, for a closer view see Fig. A1). Organic layer depth is negligible in lichen tundra and a  
126 few centimeters in dwarf-shrub tundra, meadow, and graminoid tundra. In bog, dry fen, and wet

127 fen, the organic layer depth is at least the maximum depth of the active layer, *ca.* 30–40 cm. Soil  
128 organic content reach *ca.* 40 % in tundra wetlands (Mikola et al. 2018). A section of the wet and dry  
129 fen within the EC footprint area is disturbed by vehicle tracks that create open water surfaces, and  
130 there is also an area of eroded bare-peat surface on a dry fen.

131



132

133 **Fig. 1.** a) Location of the study area in Tiksi, Yakutia, Russia, b) Land-cover map with the chamber  
134 flux measurement points (dots) and the EC mast (x), and photos of the land-cover types: c) lichen  
135 tundra with barren ground and patches of vegetation, d) dwarf-shrub tundra, e) bog, f) wet and dry  
136 fen, g) graminoid tundra, and h) meadow by the stream. See Tuovinen et al. (2019) for the EC  
137 footprint climatology.

138

139

140

141

142

143

144 **Table 1.** Soil and vegetation characteristics of the land cover types (LCT) and their proportions in  
 145 the EC impact area (90 % of the cumulative footprint).

LCT	Soil properties and plant taxa	Proportion (%) <sup>2</sup>
Lichen tundra <sup>1</sup>	Mixture of vegetated patches, stones, and bare ground. <i>Lichens</i> , e.g. genera <i>Thamnolia</i> , <i>Flavocetraria</i> , <i>Alectoria</i> , <i>Stereocaulon</i> , dwarf shrubs <i>Dryas octopetala</i> , <i>Vaccinium vitis-ideae</i> , <i>Salix polaris</i> , <i>Diapensia lapponica</i> , and forbs <i>Oxytropis</i> spp., <i>Astragalus</i> spp., <i>Pedicularis</i> spp., <i>Artemisia</i> spp., <i>Minuartia</i> sp.,	8 barren, 11 sparse vegetation
Dwarf-shrub tundra	Shallow organic layer on mineral soil ground Feather mosses, lichens, <i>Salix polaris</i> , <i>Vaccinium vitis-ideae</i> , <i>Vaccinium uliginosum</i> , <i>Dryas octopetala</i> , <i>Cassiope tetragona</i> , <i>Betula nana</i> , <i>Polygonum viviparum</i> , <i>Pedicularis</i> spp., <i>Carex</i> spp.	18
Meadow	Shallow organic layer on mineral soil ground <i>Calamagrostis</i> sp., <i>Festuca</i> sp., <i>Salix</i> spp. <i>Polygonum viviparum</i> , <i>Bistorta major</i> , <i>Polemonium</i> sp., <i>Valeriana</i> sp.	1.4
Graminoid tundra	Shallow peat layer on mineral soil ground Feather mosses, <i>Sphagnum</i> spp., <i>Carex</i> spp., <i>Eriophorum</i> spp., <i>Calamagrostis</i> spp., <i>Salix</i> spp., <i>B. nana</i> , <i>Saxifraga</i> spp., <i>Ranunculus</i> spp., <i>Bistorta major</i> , <i>Stellaria</i> sp., <i>Valeriana</i> sp., <i>Polemonium</i> sp., <i>Comarum palustre</i>	13
Bog	Dry hummock habitat at the tundra peatland <i>Sphagnum</i> spp., feather mosses, <i>Salix</i> spp., <i>Vaccinium uliginosum</i> , <i>Vaccinium vitis-ideae</i> , <i>Betula nana</i> , <i>Rhododendron tomentosum</i> , <i>Cassiope tetragona</i> , <i>Carex</i> spp., <i>Polygonum viviparum</i> , <i>Stellaria</i> sp.	23
Dry fen	Intermediate wet tundra peatland habitat <i>Sphagnum</i> spp., <i>Carex</i> spp., <i>Salix</i> spp., <i>Saxifraga</i> spp., <i>Comarum palustre</i> , <i>Epilobium</i> spp., <i>Ranunculus</i> spp., <i>Pedicularis</i> spp., <i>Stellaria</i> sp.	10
Wet fen	Wet tundra peatland habitat with open pools <i>Brown mosses</i> , <i>Carex</i> spp., <i>Eriophorum</i> spp., <i>Ranunculus</i> sp., <i>Caltha palustris</i> , <i>Pedicularis</i> sp., <i>Saxifraga</i> sp.	15

146 <sup>1)</sup> Combined land-cover types bare and lichen tundra in Juutinen et al. (2017), Mikola et al. (2018),  
 147 Tuovinen et al. (2019), <sup>2)</sup> Proportion within the 90% coverage of the mean EC footprint area during  
 148 the growing season of 2014 (Tuovinen et al. 2019).

151        2.2  $CO_2$  and  $CH_4$  flux measurements

152        Fluxes of  $CO_2$  and  $CH_4$  were measured using static chambers equipped with a fan and set on pre-  
 153        installed collars of 50 cm  $\times$  50 cm. The measurement points (collars) were set to cover the  
 154        heterogeneity in land cover, and in each study year, there were 1–4 measurement points per each  
 155        LCT (Table 2). Most of the data were collected during a study campaign in July 15 – August 16,  
 156        2014 (12 collars). The growing season had started earlier due to a warm period and daily mean air  
 157        temperature stayed over 5 °C since July 5 (Fig. 2 and Tuovinen et al. 2019). Net ecosystem  
 158        exchange of  $CO_2$  (NEE) and ecosystem respiration of  $CO_2$  in dark (ER) were measured using  
 159        transparent and opaque chambers (transparent chamber covered with a hood), respectively, allowing  
 160        the partitioning of ecosystem gross photosynthesis (Pg) and ER. Fluxes of  $CH_4$  were determined  
 161        from closures of both transparent and opaque chambers, but because there was no difference  
 162        between them when performed consecutively, the data from opaque chamber measurements were  
 163        used for flux calculations. In addition,  $CH_4$  fluxes were measured during shorter campaigns in 2012,  
 164        2013, 2016, and 2019 (Table 2). These data also included vehicle track disturbance plots and an  
 165        eroded bare-peat surface, which were measured in 2019.

166        **Table 2.** Measurement periods, measured fluxes ( $CH_4$ , ER, NEE), and number of measurement  
 167        points and observations (points, observations) in each land cover type (LCT) across the study years.

	2012	2013	2014	2016	2019
LCT	Jul 18–21	Jul 5–Sep 3	Jul 15–Aug 16	May 30, Aug 4–5, Sep 13–14	Aug 28–Sep 1
	$CH_4$	$CH_4$	ER, NEE, $CH_4$	$CH_4$	$CH_4$
Wet fen	4, 4	6, 22	3, 107	3, 27	5, 72
Vehicle track					2, 30
Dry fen	2, 2	4, 11	3, 107	3, 14	2, 26
Bare peat					1, 15
Bog	2, 2	3, 7	1, 36		1, 13
Meadow	1, 1	2, 6	2, 62		
Dwarf-shrub tundra	1, 1		1, 36	1, 1	
Lichen tundra		1, 3	2, 67	2, 18	2, 29
Snow and ice <sup>1</sup>				2, 2	

<sup>1</sup>Measured only on May 30, 2016.

168 In 2012 and 2013, four air samples were taken from the chambers using syringes. The  
169 samples were stored in glass vials prior to the analysis. First, a vial was flushed with the sample and  
170 then filled to over-pressure. The samples were analyzed for CH<sub>4</sub> concentration using a TSVET 500-  
171 M gas chromatograph (Chromatek, Russia) with a flame ionization detector at the laboratory of the  
172 Voeikov Main Geophysical Observatory within a month from sampling. Each measurement was  
173 accompanied by calibration using standard gas mixtures with the NOAA2004 scale. The vials were  
174 tested prior to the field sampling using a standard gas: after two weeks, the vials were still over-  
175 pressurized and sample CH<sub>4</sub> concentrations were within  $\pm 3$  ppb of the initial standard gas  
176 concentration. Since July 2014, CH<sub>4</sub> and CO<sub>2</sub> concentrations inside the chambers were recorded  
177 every second during closures of about 5 min using a gas analyzer (DLT-100, Los Gatos Research,  
178 Inc., San Jose, CA, USA) (see Fig. A2 for examples). Gas fluxes between the ecosystem and the  
179 atmosphere were calculated from the phase of linear concentration change in the chamber head  
180 space over time and accounting for temperature, volume, and atmospheric pressure. Concentration  
181 change during each chamber closure was evaluated visually for determining the closure start time  
182 and to remove cases showing nonlinearity due to leaks, ebullition, or saturation. The first data  
183 points were generally neglected when determining the slope of concentration change over time, and  
184 the cases with a linear concentration change had a coefficient of determination ( $R^2$ )  $> 0.9$ . For near  
185 zero flux cases smaller  $R^2$  values were accepted to not ignore those cases. There were a few  
186 ebullition cases at the vehicle track measurement points that had only sparse or no vegetation cover,  
187 and those measurements were included in the final data. When determining NEE fluxes measured  
188 using the transparent chamber, the data were screened for variation in photosynthetically active  
189 photon flux density (PPFD), measured during the chamber closure, and rejected if the PPFD  
190 variation exceeded 100  $\mu\text{mol m}^{-2} \text{s}^{-1}$  during the measurement.

191 The fluxes of CO<sub>2</sub> and CH<sub>4</sub> were also measured by the micrometeorological EC  
192 method, which provides continuous data of the atmosphere-biosphere fluxes averaged on an

193 ecosystem scale. The EC system consisted of a three-dimensional sonic anemometer (USA-1,  
194 METEK GmbH, Elmshorn, Germany), a closed-path CH<sub>4</sub> analyzer (RMT-200, Los Gatos Research,  
195 Inc., San Jose, CA, USA), and a closed-path CO<sub>2</sub>/H<sub>2</sub>O analyzer (LI-7000, LI-COR, Inc., Lincoln,  
196 NE, USA). The fluxes were calculated as 30-min averages and processed using standard methods  
197 (Aubinet et al. 2012). The EC measurement system and the post-processing procedures have been  
198 presented in more detail by Tuovinen et al. (2019).

199 Supporting meteorological measurements including air temperature (T<sub>air</sub>) (HMP,  
200 Vaisala), soil temperature (T<sub>soil</sub>) (IKES, Nokeval), PPFD (PQS1, Kipp & Zonen), and water table  
201 level relative to the ground surface (WT) (8438.66.2646, Trafag) were collected by a Vaisala QML  
202 datalogger as 30-min averages. We also present meteorological data for the period 2011–2019 to  
203 relate the conditions during the measurement campaign in July 15 - August 16, 2014, and the CH<sub>4</sub>  
204 flux campaigns in 2012, 2013, 2014, 2016, and 2019, to longer-term variations.

205

### 206 2.3 Vegetation and Topographic Wetness Index

207 On a site level, vegetation and soil characteristics were inventoried in plots assigned into a  
208 systematic grid outside the area covered by the gas flux measurement points in 2014 (see Juutinen  
209 et al. 2017; Mikola et al. 2018). The projection cover (%) of plant species and species groups, and  
210 the mean canopy height of each species group were recorded. Seven species groups were included  
211 in the inventory: *Sphagnum* mosses, feather mosses, brown mosses, dwarf shrubs, *Betula nana*,  
212 *Salix* species, forbs, and graminoids. A subset of the plots was harvested, and vascular plant leaves  
213 were scanned to determine the one-sided LAI to find an empirical relationships between LAI and  
214 %-cover and canopy height to estimate the LAI in the collars (see Juutinen et al. 2017). In the  
215 collars, the projection cover and canopy height of each species group were recorded weekly during  
216 the gas flux measurement campaign in July 15–August 16, 2014. Because there were no  
217 observational vegetation data for the other years than 2014, the green chromatic coordinate (GCC)

218 was used as a proxy for the amount of green above-ground vascular plants (e.g. Richardson 2019).  
219 GCC was calculated from the digital numbers of red (R), green (G), and blue (B) color channels as  
220 the proportion of green in the RGB images,  $GCC = G/(R+G+B)$ , of the vegetation inside the collars.  
221 The photographs were taken at the time of measurements. We determined an empirical relationship  
222 between LAI and GCC by using a data set of harvested plots with digital photographs and measured  
223 LAI data (n=91). For the LAI estimation, we used a linear relationship ( $R^2 = 0.46$ ,  $p < 0.001$ )  
224 between LAI and GCC determined using the entire data set (see Fig. A3 for the data and equation).

225 To quantify the potential soil wetness at each measurement point, we calculated the  
226 mean topographic wetness index (TWI) value based on a 2 m spatial resolution digital elevation  
227 model (Mikola et al. 2018). To characterize differences between growing seasons as manifested by  
228 vegetation greenness, the MODIS Normalized Difference Vegetation Index (NDVI) with 16-day  
229 temporal and 500 m spatial resolution was calculated for a circular area with a 300 m radius from  
230 the flux tower using Google Earth Engine (Gorelick et al. 2017). NDVI was derived for 2011–2019  
231 to place the measurement years in the context of year-to-year variation in weather.

232

#### 233 2.4 Data analyses

234 When examining the role of the LCTs in  $CO_2$  and  $CH_4$  exchange, we applied the land cover  
235 classification presented in Mikola et al. (2018). The data collected in July 15 – August 16, 2014  
236 were used for examining gas exchange in relation to the variation in LAI, GCC, WT, and TWI  
237 among the collars. The light-normalized Pg and NEE at  $PPFD = 800 \mu\text{mol m}^{-2} \text{s}^{-1}$  ( $Pg_{800}$  and  
238  $NEE_{800}$ , respectively), were estimated by fitting a hyperbolic response function of  $CO_2$  vs PPFD  
239 utilizing the ER and NEE flux data:

240

241  $NEE = ER - Pg_{max} \times PPFD / (\beta + PPFD)$ , (1)

242

243 where  $Pg_{max}$  is the asymptotic maximum of photosynthesis, and  $\beta$  is the half-saturation PPFD.  
244 Fluxes of CH<sub>4</sub> are expressed as temporally averaged per each collar. We used a sign convention  
245 where a positive value means net release to the atmosphere and a negative value denotes net uptake  
246 by the ecosystem. Fluxes of CH<sub>4</sub> measured over all study years, 2012–2019, were averaged for each  
247 LCT.

248 Regression analyses were used to test the relationships between gas flux estimates and  
249 vascular LAI, GCC, WT, and TWI. All CH<sub>4</sub> flux data from the years 2012–14, 2016, and 2019 were  
250 used to quantify the mean growing season CH<sub>4</sub> flux for each LCT and examine the relationship  
251 between CH<sub>4</sub> and GCC and TWI. To find the main factors and gradients in the plant community,  
252 gas flux, and environmental variables data measured in the flux collars in 2014, we performed a  
253 detrended correspondence analysis (DCA) of the species group data with post-hoc fit of  
254 environmental variables, including gas fluxes, WT, LAI, GCC, elevation, and thaw depth as  
255 supplementary variables. The DCA was performed on logarithmically transformed, centered species  
256 data (species or species groups) using Canoco 5 (Ter Braak and Šmilauer 2012).

257 We compared the LCT-specific flux estimates based on the chamber measurements  
258 with the estimates based on EC measurements over the same period. Partitioning of the EC-based  
259 CO<sub>2</sub> fluxes to Pg and ER and estimates of Pg<sub>800</sub> and NEE<sub>800</sub> were calculated similarly to that of  
260 chamber data using Eq. (1). The EC flux data were classified into five wind sectors (30–125°, 125–  
261 185°, 185–239°, 239–310°, 310–360°) based on the mean EC flux footprint, modeled for the  
262 growing of 2014 by Tuovinen et al. (2019). The sectors distinguished areas dominated by different  
263 LCTs, especially tundra heaths and wetlands, and similarly those with a large and small vascular  
264 LAI. For each sector, the footprint-weighted areal proportions of LCTs and mean vascular LAI  
265 were derived from the high spatial resolution LCT and LAI maps (Mikola et al. 2018). For this  
266 comparison, sector averages of Pg<sub>800</sub>, ER, NEE<sub>800</sub>, and CH<sub>4</sub> flux were calculated from the chamber  
267 data by weighting the LCT-specific flux estimates with the above-mentioned LCT proportions in

268 each sector. Because there were no chamber measurement points within graminoid tundra, we  
269 applied wet fen (for  $\text{CO}_2$ ) and dry fen (for  $\text{CH}_4$ ) flux estimates for the graminoid tundra based on  
270 the observed similarities in LAI and soil wetness, respectively. Overall, graminoid tundra can be  
271 considered part of the fen continuum in terms of soil characteristics (high organic content) and  $\text{CH}_4$   
272 exchange (Mikola et al. 2018, Tuovinen et al. 2019).

273 Finally, to synthesize the  $\text{CO}_2$  and  $\text{CH}_4$  exchange variability across the tundra, we  
274 upscaled the LCT-specific average  $\text{NEE}_{800}$ ,  $\text{Pg}_{800}$ , ER, and  $\text{CH}_4$  flux (2014 data) to the 35.8 km<sup>2</sup> area  
275 surrounding our study site, for which a LCT map was produced by Mikola et al. (2018).

276

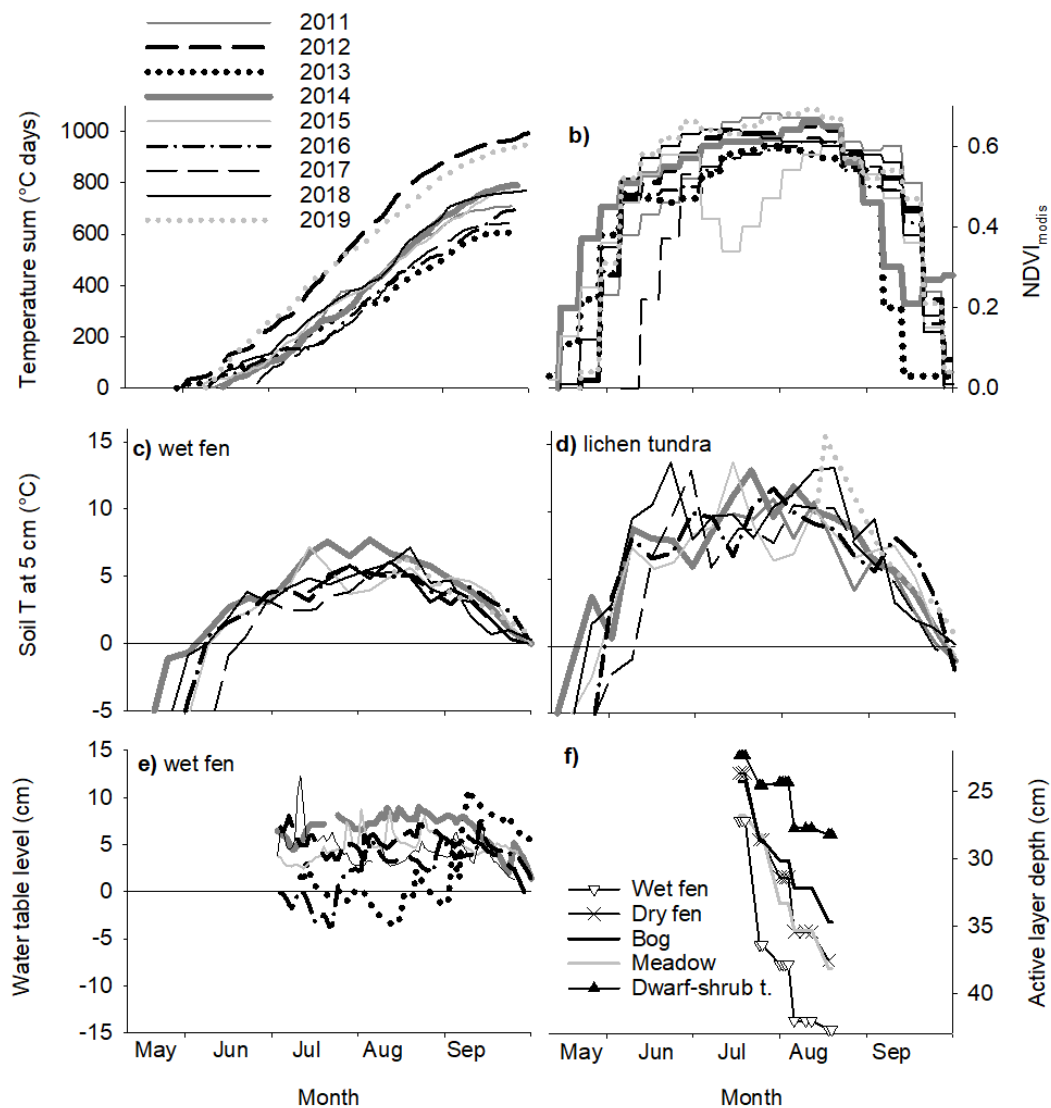
### 277 3 Results

#### 278 3.1 Environmental conditions

279 In 2014, when we collected most of the flux data, temperature sum accumulation (with a 0 °C  $\text{T}_{\text{air}}$   
280 threshold) was near-average during the thaw period (the period when soil surface temperature was  
281 continuously above 0 °C), but the spring and mid-growing season were warmer than on average  
282 (Fig. 2a). The average air temperature was 15 °C during the gas flux measurements. Accordingly,  
283 the MODIS NDVI showed an early start of greening (Fig. 2b), and vegetation development had  
284 already started at the beginning of the measurement period. In 2011–2019, which included the other  
285  $\text{CH}_4$  measurement years, the thaw period lasted for 74–124 days, creating a temperature sum range  
286 of 642–1003 °C days (Fig. 2a). Surface soils thawed between May 28 and July 9 and froze again  
287 between September 21 and October 1. Among the observation years, the years 2012 and 2019 had  
288 notably longer and warmer thaw periods than the other years. The driest habitat, lichen tundra, with  
289 least snow accumulation, thawed 10–15 days earlier than the other habitats, and had a ca. 3 °C  
290 higher soil temperature than the wet fen at the depth of 5 cm (Fig. 2c–d). Water table level,  
291 measured at a wet fen location, showed only subtle interannual variation (Fig. 2e). In 2014, the  
292 active layer depth, measured over the measurement period close to the collars, was deepest in the

293 end of August, reaching *ca.* 40 cm in wet fen, and remained < 30 cm in the dry dwarf-shrub tundra  
 294 (Fig. 2f). Lichen tundra had rocks underneath the loose surface layer, which made it impossible to  
 295 measure the actual thaw depth.

296



297

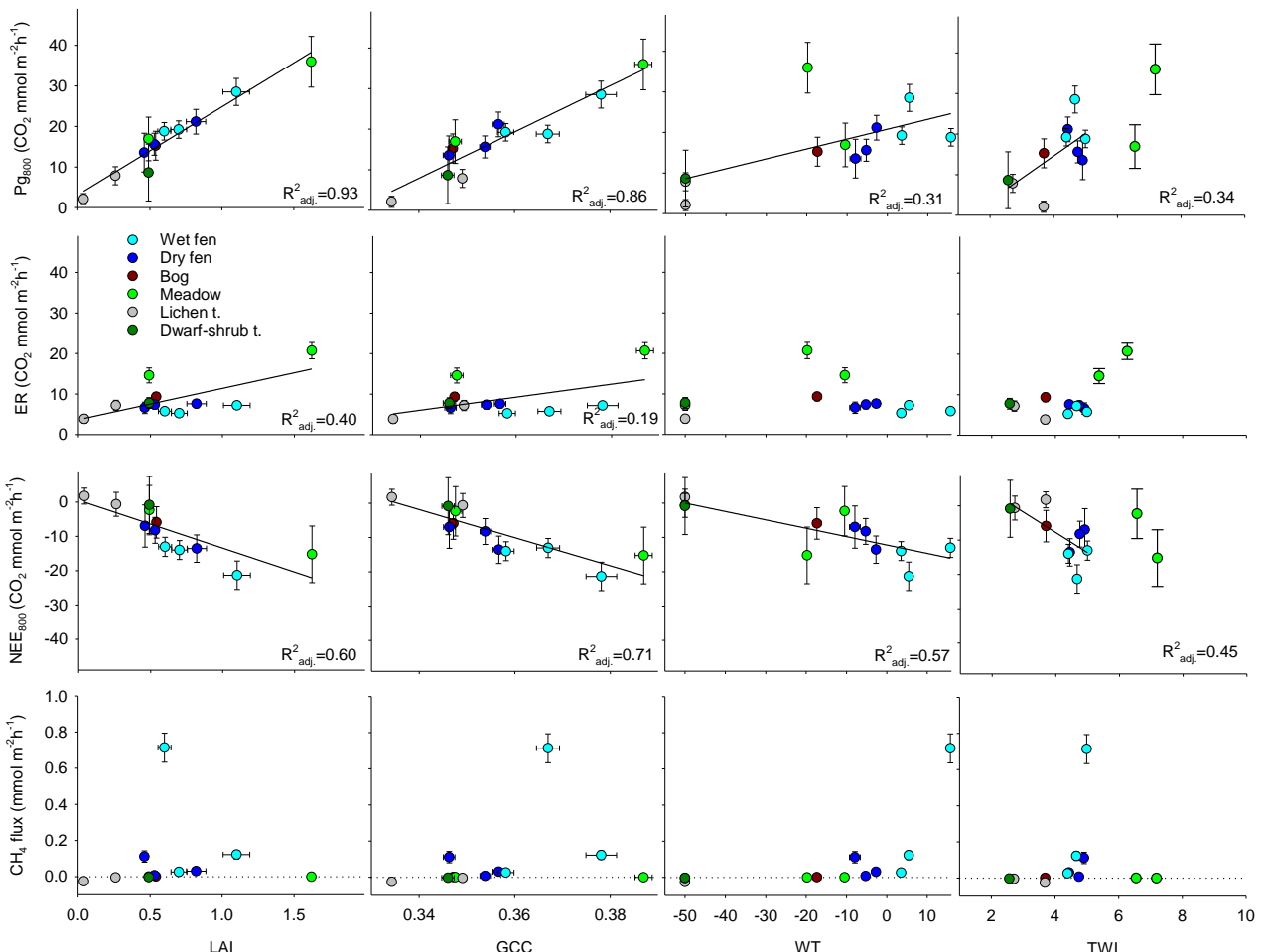
298 **Fig. 2.** **(a)** Air temperature accumulation with the threshold surface  $T_{\text{soil}}$  and  $T_{\text{air}}$  of 0  $^{\circ}\text{C}$ , **b)**  
 299 seasonal dynamics of NDVI in the study area, 16 d MODIS data, **c)** weekly means of soil  
 300 temperature at depth of 5 cm in wet fen and **d)** in lichen tundra, **e)** water-table level relative to the  
 301 ground surface in wet fen, and **f)** LCT means of thaw depth in the measurement collars in 2014.  
 302 Rocks in the ground prevented detecting the thaw depth of lichen tundra.

### 303 3.2 Exchange of $\text{CO}_2$ and $\text{CH}_4$

304 Among different LCTs,  $\text{Pg}_{800}$  varied from about 5  $\text{mmol m}^{-2} \text{h}^{-1}$  in the lichen tundra to 22 and 27  
 305  $\text{mmol m}^{-2} \text{h}^{-1}$  in the wet fen and meadow, respectively.  $\text{Pg}_{800}$  was strongly and positively correlated

306 with the vascular plant LAI and the greenness index GCC (Fig. 3). There was also a positive  
307 correlation between Pg<sub>800</sub> and both WT and TWI, possibly because the highest LAI occurred at the  
308 wet fen and meadow plots. However, the TWI values for the two meadow plots located on an  
309 elevated bank of the stream were disproportionately high in relation to the WT at the plots, probably  
310 because of insufficient locational accuracy or an artefact in the digital elevation model. Ecosystem  
311 respiration was highest in the two meadow plots, on average 18 mmol m<sup>-2</sup> h<sup>-1</sup>. The relationship  
312 between ER and LAI was weaker than between Pg<sub>800</sub> and LAI (Fig. 3). NEE<sub>800</sub> varied from about  
313 zero in the lichen tundra plots to a net CO<sub>2</sub> uptake of 16 mmol m<sup>-2</sup> h<sup>-1</sup> in the meadow and wet fen  
314 plots. NEE<sub>800</sub> was more tightly linked to Pg<sub>800</sub> than to ER and was correlated with LAI, GCC, WT,  
315 and TWI (Fig. 3).

316 There was substantial consumption of the atmospheric CH<sub>4</sub> in the barren tundra (mean  
317 -0.018 ± standard error 0.002 mmol m<sup>-2</sup> h<sup>-1</sup>) and in vegetated lichen tundra (-0.006 ± 0.002 mmol m<sup>-</sup>  
318 <sup>2</sup> h<sup>-1</sup>) (Figs. 4 and 5). Minor consumption occurred in the bog, meadow, and dwarf-shrub tundra  
319 plots (mean -0.001 ± standard error 0.0008 mmol m<sup>-2</sup> h<sup>-1</sup>), while efflux to the atmosphere was  
320 observed in the dry fen and wet fen plots (means 0.05 and 0.16 mmol m<sup>-2</sup> h<sup>-1</sup>, respectively; Figs. 4  
321 and 5). The eroded bare-peat plot within the dry fen habitat and the vehicle-track plots in wet fen  
322 had equally high emissions as the fens (up to 0.2 mmol m<sup>-2</sup> h<sup>-1</sup>). Variation among the plot means of  
323 CH<sub>4</sub> flux (Fig. 3 for 2014, Fig. 5 for all years) was related to WT, and CH<sub>4</sub> emissions occurred  
324 when TWI was > 4. The two meadow plots that showed net consumption of CH<sub>4</sub> had an  
325 unrealistically high TWI relative to their WT (see above and Figs. 3 and 5). Variation in CH<sub>4</sub> fluxes  
326 was incoherently related to variation in LAI and GCC because of the high emission cases in plots  
327 with little vegetation, including the wettest wet fen plot, vehicle-track, and bare-peat plots (Fig. 5).



328

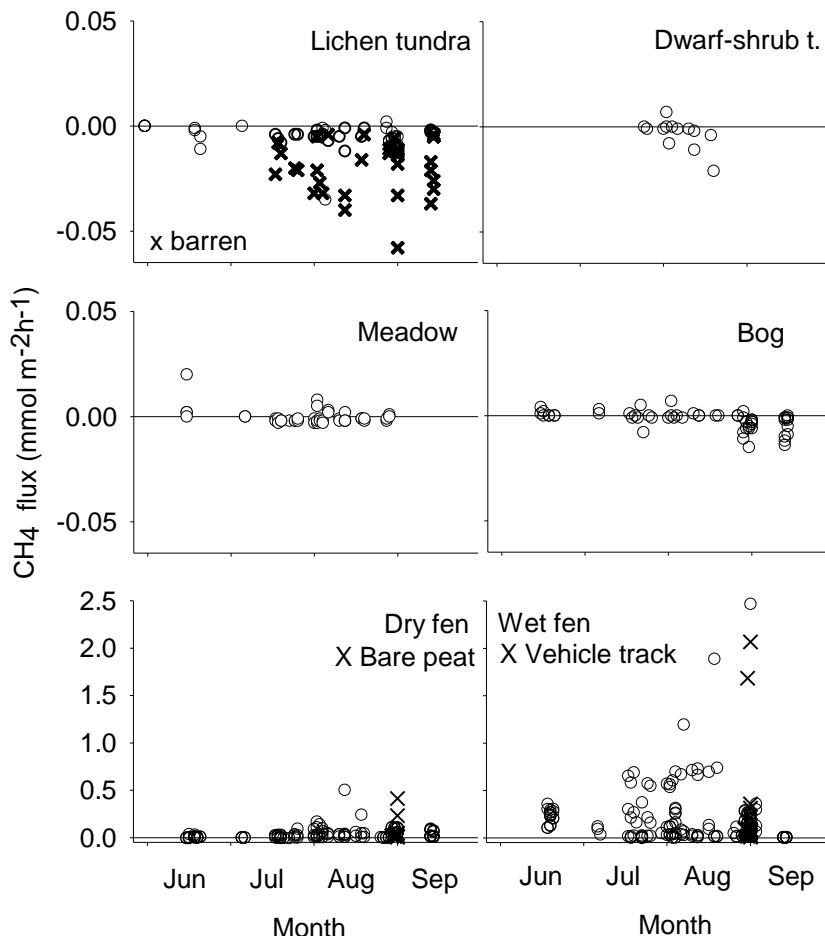
329

330 **Fig. 3.** Variation in estimates of Pg<sub>800</sub>, ER, NEE<sub>800</sub> (Eq. 1) and collar means of CH<sub>4</sub> fluxes in  
 331 relation to variation in collar means of LAI, GCC, WT, and TWI in July 6–August 16, 2014. Error  
 332 bars denote the standard error of estimate. Fitted regression lines and adjusted coefficients of  
 333 determination ( $R^2_{adj.}$ ) are included for the significant linear relationships. The two meadow plots  
 334 were not included in the TWI regressions.

335

336

337

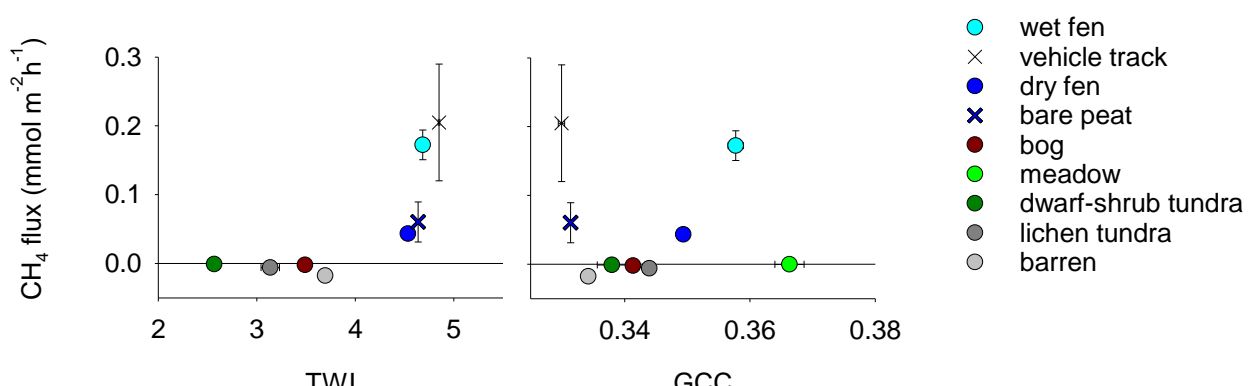


338

339 **Fig. 4.** Instantaneous  $\text{CH}_4$  fluxes in each LCT. The data are a composite of all study years.  
 340 Barren surfaces are indicated among the lichen tundra data. The eroded bare-peat and vehicle-track plots  
 341 (×) are plotted as part of the dry fen and wet fen data, respectively. Note that the panel groups have  
 342 different y-axis scales.

343

344

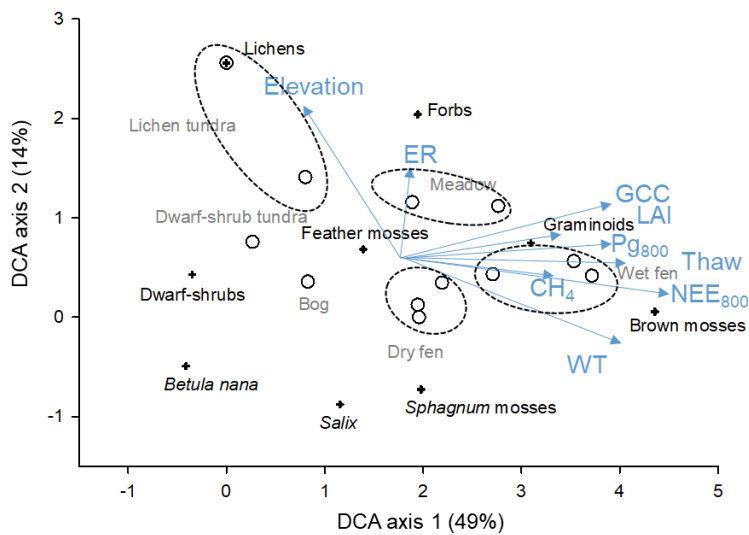


345

346 **Fig. 5.** LCT mean ( $\pm \text{SE}$ )  $\text{CH}_4$  fluxes in relation to LCT mean ( $\pm \text{SE}$ ) TWI (excluding the meadow)  
 347 and GCC. Data from years 2012–2019.

348

349 The DCA ordination of species groups with a post-hoc fit of environmental variables  
 350 (elevation, WT, thaw depth, LAI, GCC, and CO<sub>2</sub> and CH<sub>4</sub> exchange) showed that species  
 351 distributed along a moisture gradient. Axis 1 explained 49 % of the variation in the species data and  
 352 distinguished the wet and dry LCTs from wet fen to lichen tundra (Fig. 6). Graminoids and brown  
 353 mosses occurred in the wet end of the gradient, while dwarf-shrubs, *Betula nana*, and lichens  
 354 occurred in the dry end of it. The barren plot (the other lichen tundra plot) with its negligible  
 355 vegetation differed most from the other plots. Axis 2 explained additional 14 % of the variation in  
 356 the species data (Fig. 6). The supplementary variables WT, vascular plant LAI, thaw depth, GCC,  
 357 Pg<sub>800</sub>, NEE<sub>800</sub>, and CH<sub>4</sub> fluxes correlated positively with Axis 1 having post-hoc correlations (r) of  
 358 0.6–0.9, as derived from the DCA-weighted correlation matrix. In turn, plot's elevation and ER had  
 359 positive correlations with Axis 2 (r = 0.8 and 0.4, respectively).



360  
 361 **Fig. 6.** DCA ordination diagram based on species (species groups) data from the measurement  
 362 collars in 2014. The explained variation in the species data is indicated for the axes. In the plot, the  
 363 scores of species groups (cross), sample plots (open symbols), and post-hoc fits of the  
 364 supplementary variables (arrows, blue type) mean CH<sub>4</sub>, Pg<sub>800</sub>, ER, NEE<sub>800</sub>, thaw depth (Thaw),  
 365 water table relative to the ground surface (WT), green chromatic coordinate (GCC), vascular plant  
 366 LAI, and elevation above sea level (Elevation). Land-cover types of the sample plots are indicated  
 367 (grey type) and plots assigned to the same LCTs are circled.

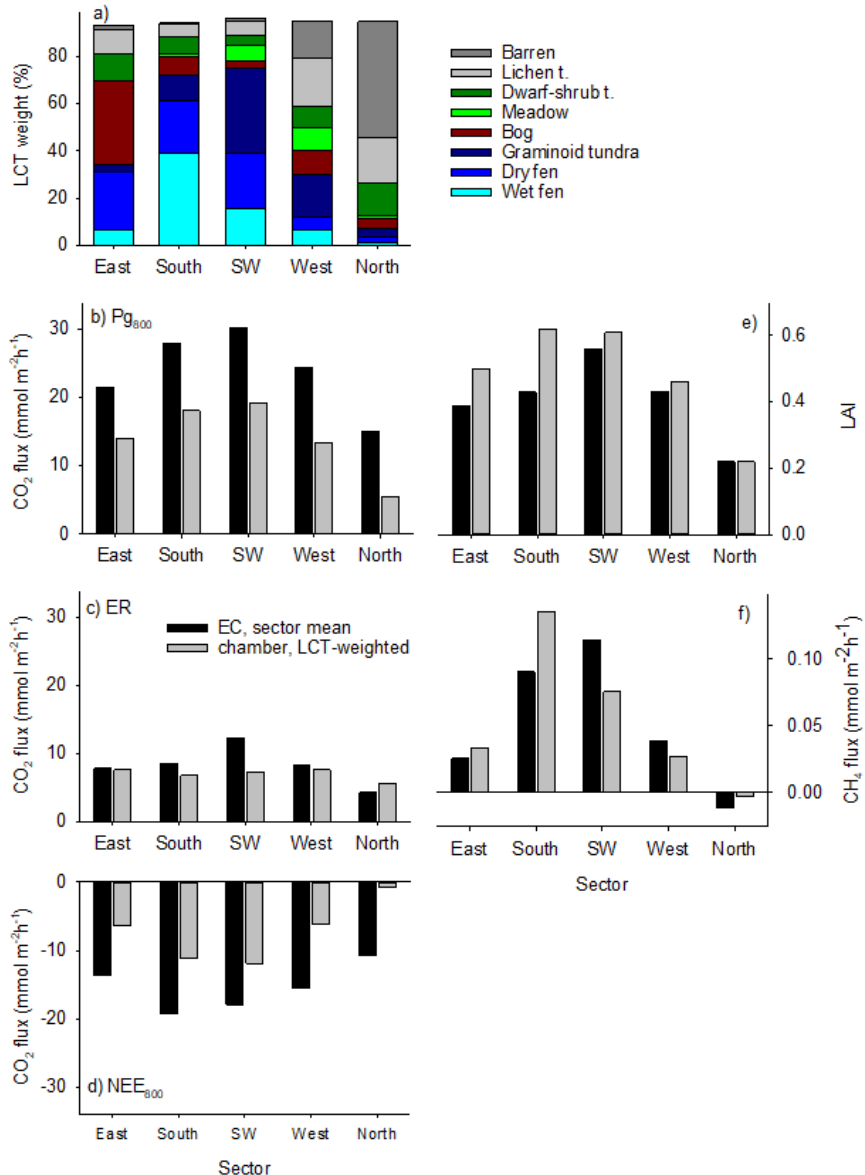
368

369 In both the southern and south-western wind sectors (125–185° and 185–239°),  
370 vegetation mainly consisted of graminoids, as the LCTs dry fen, wet fen, graminoid tundra, and  
371 meadow comprised 80 % of the total EC footprint-weighted area (Fig. 7a). The northern sector  
372 (310–360°) was characterized by lichen tundra and bare ground that accounted for 68 % of the  
373 footprint-weighted LCT areas, while all the other LCTs covered less than 18 % in total. The other  
374 wind direction sectors had more even LCT distributions. The differences between the sectors were  
375 similar in the EC-based and spatially weighted chamber-based averages of CO<sub>2</sub> exchange (Fig. 7b–  
376 d). Both Pg<sub>800</sub> and NEE<sub>800</sub> were largest in the southern and south-western sectors and clearly  
377 smallest in the barren–lichen tundra-dominated sector in the north. The chamber-based estimates of  
378 CO<sub>2</sub> exchange were, however, lower: on average, Pg<sub>800</sub> was 57 %, ER 93 %, and NEE<sub>800</sub> 44 % of  
379 the mean EC-based fluxes among the wind direction sectors.

380 The southern and south-western wind sectors with abundant dry and wet fens and  
381 graminoid tundra had clearly the largest CH<sub>4</sub> fluxes (Fig. 7f). The estimate based on chamber  
382 measurements was 30 % and 50 % larger than the mean EC-based flux in the east sector (dominated  
383 by dry fen and bog) and south sector (dominated by dry and wet fen), respectively. In contrast, the  
384 chamber-based estimate was smaller than the EC flux for the other sectors, which were dominated  
385 by graminoid tundra, lichen tundra, and barren ground. Both the EC- and chamber-based  
386 measurements showed consumption of atmospheric CH<sub>4</sub> in the northernmost sector, of which  
387 barren ground and lichen tundra covered 50 % and 20 %, respectively. The mean EC flux was three  
388 times the chamber-based estimate.

389 Within the extended study area of 35.8 km<sup>2</sup>, the LCT-weighted mean NEE<sub>800</sub> was -4.6  
390 mmol m<sup>-2</sup> h<sup>-1</sup> (uptake relative to the atmosphere). The corresponding mean Pg<sub>800</sub> was 11 mmol m<sup>-2</sup>  
391 h<sup>-1</sup>, and CH<sub>4</sub> flux 0.05 mmol m<sup>-2</sup> h<sup>-1</sup> (Table 3). Relative to their spatial cover (28 % in total), wet and  
392 dry fens were disproportionately important for the landscape-level Pg<sub>800</sub>, NEE<sub>800</sub>, and CH<sub>4</sub> emissions,  
393 because the fens contributed 47 % of total Pg<sub>800</sub> and 74 % of NEE<sub>800</sub>, and were the dominant source

394 of CH<sub>4</sub> emission (Table 3). Consumption of CH<sub>4</sub> by barren and lichen tundra, dwarf-shrub tundra,  
 395 and meadow tundra soils contributed -9 % of the CH<sub>4</sub> balance, and the barren ground dominated the  
 396 sink.



397

398 **Fig. 7.** Footprint-weighted mean contribution of each LCT to the EC measurements divided into  
 399 wind direction sectors (a), and comparison of EC and chamber-based sector means of CO<sub>2</sub>  
 400 exchange (Pg<sub>800</sub>, ER, and NEE<sub>800</sub>) (b-d) vascular plant LAI (e), and CH<sub>4</sub> fluxes (f). The chamber-  
 401 based data are weighted by the LCT proportions shown in panel a. All data were measured in 2014.  
 402 Map of LAI (Tuovinen et al., 2019) and the LAI measured in the collars were used to estimate the  
 403 EC- and chamber-related sector means, respectively, in panel e.

404

405

406

407 Table 3. Land-cover type distribution in the mapped 35.8 km<sup>2</sup> area (Mikola et al. 2018), spatially  
 408 weighted and LCT-specific means of Pg<sub>800</sub>, ER, NEE<sub>800</sub>, and CH<sub>4</sub>, and proportions of LCTs in  
 409 landscape totals of Pg<sub>800</sub>, NEE<sub>800</sub>, and CH<sub>4</sub> fluxes. Standard error of mean (SE) is shown for the  
 410 LCT-specific estimates. Data period: July 15 – August 16, 2014.

LCT	Area	Pg <sub>800</sub>		ER		NEE <sub>800</sub>		CH <sub>4</sub> flux		Pg <sub>800</sub>	NEE <sub>800</sub>	CH <sub>4</sub> flux
	(%)	(mmol m <sup>-2</sup> h <sup>-1</sup> )	(%)	(%)	(%)							
Mean <sup>1</sup>		11.2		6.6		-4.6		0.05				
		mean	SE	mean	SE	mean	SE	mean	SE			
Wet fen	16.4	21.9	2.5	6.4	0.7	-15.5	3.2	0.29	0.05	32.1	55.1	94.5
Dry fen	11.6	14.6	3.5	7.0	1.1	-7.6	4.6	0.05	0.01	15.1	19.1	11.2
Gram. t. <sup>2</sup>	3.4	21.9	2.5	6.4	0.7	-15.5	3.2	0.05	0.01	6.7	11.4	3.3
Bog	9.1	15.3	3.6	9.3	1.0	-5.9	4.6	0.0001	0.0005	12.4	11.7	0.03
Meadow	0.4	26.4	5.8	17.7	1.9	-8.8	7.7	-0.001	0.0004	0.9	0.8	-0.01
Dwarf-s. t.	27.4	8.6	7.0	7.8	1.3	-0.8	8.3	-0.003	0.0015	21.1	5.0	-1.8
Lichen t.	11.1	5.0	2.2	5.5	1.3	0.5	3.5	-0.005	0.001	4.9	-1.3	-1.1
Barren	15.3	5.0	1.4	5.5	1.0	0.5	2.3	-0.020	0.003	6.8	-1.8	-6.1
Water	5.3	NA		NA		NA		NA				

411 <sup>1</sup> area-weighted mean, <sup>2</sup>Graminoid tundra fluxes estimated using values for wet fen (CO<sub>2</sub>) and dry fen (CH<sub>4</sub>)

412

## 413 2 Discussion

414 The studied tundra site in Tiksi in northeastern Siberia has heterogeneous land cover, which is  
 415 reflected as equally heterogeneous CO<sub>2</sub> and CH<sub>4</sub> exchange. We found that the LAI of vascular  
 416 plants was a robust predictor of Pg<sub>800</sub> and NEE<sub>800</sub> across the LCTs. On the one hand, due to the  
 417 distribution of species and LAI, the tundra wetlands had a disproportionate role in the landscape-  
 418 level CO<sub>2</sub> uptake capacity. The fens also dominated the landscape's CH<sub>4</sub> emissions. On the other  
 419 hand, our results highlight the high CH<sub>4</sub> consumption rates within the dry tundra areas. The  
 420 consumption of the atmospheric CH<sub>4</sub> by dry tundra was -9 % of the total CH<sub>4</sub> balance within this  
 421 landscape, and the consumption rate of the barren was much higher than in other dry tundra habitats.  
 422 This finding is in agreement with other studies and suggest distinguishing non-vegetated dry tundra  
 423 habitats when upscling CH<sub>4</sub> fluxes (Table 4). In Tiksi, the barren was characterized by sand and  
 424 rocks underlain by chists (Fig. A1). The consumption of CH<sub>4</sub> was smaller if the sand and stones

425 were partly covered with vegetation and, in lichen tundra, with a thin organic layer (Figs. 5 and  
426 A1).

427 The land-cover categorical approach serves to distinguish the basic features of spatial  
428 variation in CO<sub>2</sub> and CH<sub>4</sub> fluxes. The extreme ends of the moisture and vegetation gradients from  
429 barren to wet fen are clearly distinguishable, also in terms of CO<sub>2</sub> and CH<sub>4</sub> exchange (Fig. 6).  
430 Overall, microrelief, moisture gradient, vegetation types and ecosystem functions are connected.  
431 Barren areas are wind swept having minimal snow accumulation, while in wet depressions snow  
432 accumulation further increases soil moisture (Fig. 6, Callaghan et al. 2011). Nevertheless, the  
433 spatial extrapolation of fluxes is clearly sensitive to a small number of chamber measurement points  
434 as there is large within-LCT variation, as observed in the wet fen and meadow data, which  
435 originates from the plot-to-plot variation in LAI. The LCTs share common features and form a  
436 continuum as shown by the DCA ordination (Fig. 6). Mikola et al. (2018) used a larger data set  
437 from Tiksi and also found that the neighboring LCTs overlapped in terms of soil properties and  
438 vegetation. Despite the limited number of observations, our conclusions drawn from the chamber  
439 data are, corroborated by the temporally matching section of EC data, which show similarity to the  
440 chamber data (Fig. 7). Furthermore, the statistical analysis of EC data by Tuovinen et al. (2019)  
441 showed that it is possible to find significant differences between different LCT categories  
442 representing high and low CH<sub>4</sub> emitters and CH<sub>4</sub> sinks. However, for spatial modeling of ecosystem  
443 functions, maps of key variables, such as LAI and WT, that drive CO<sub>2</sub> and CH<sub>4</sub> exchange would be  
444 preferable to categorical LCT classification (Räsänen et al. 2021).

445 The spatial pattern of the growing season Pg<sub>800</sub> and NEE<sub>800</sub> was strongly related to the  
446 corresponding pattern of the LAI of vascular plants (Figs. 3 and 4). Hence, the abundance of  
447 graminoid (Cyperaceae and Poaceae) vegetation was associated with a large NEE<sub>800</sub>, which varied  
448 from near zero in lichen tundra up to 25 mmol m<sup>-2</sup> h<sup>-1</sup> in wet fen. Ecosystem respiration had a  
449 smaller role than Pg in determining NEE, but we note that our data cover only a section of the

450 growing season with warmer temperatures and half to full-grown vegetation. The importance of ER  
451 is likely to be different when considering the full annual balance (*e.g.*, Hashemi et al. 2021). While  
452 our data represent only the growing season, a similar relationship has also been found between the  
453 annual NEE and LAI at a tundra site with a mixture of wet and dry tundra in northeastern Europe  
454 (Marushchak et al. 2013), in a multi-site EC study in Alaskan tundra (McFadden et al. 2003), in  
455 Canadian low arctic tundra wetlands (Lafleur et al. 2012), and across tundra sites (Street et al. 2007;  
456 Shaver et al. 2007).

457 The magnitude of Pg<sub>800</sub> and NEE<sub>800</sub> in the fen and meadow plots of this study were  
458 similar to the maximum Pg and NEE found in tundra wetland in Seida in northeastern Europe  
459 (Marushchak et al. 2013), at low tundra wetland sites in eastern Canada (Lafleur et al. 2012), and at  
460 a wetland-dominated but more continental site (with an equally long growing season) in  
461 northeastern Siberia (van der Molen et al. 2007). The vegetation and Pg<sub>800</sub> of lichen tundra and  
462 dwarf-shrub tundra in our study resembled those observed within the polygon rim habitat of the  
463 polygon tundra in the Lena River delta, while those of meadow, dry fen, and wet fen resembled the  
464 wet polygon center habitats (Eckhardt et al. 2019). In our study, the variation of ecosystem  
465 respiration resulted from the variation in vascular plant LAI, soil organic content, and water  
466 saturation: the highest ER occurred in mineral soil meadow with high LAI, suggesting substantial  
467 autotrophic respiration, and likely deep rooting and large root biomass contributing to the  
468 ecosystem respiration (Fig. 3).

469 Our chamber-based estimate of the average CH<sub>4</sub> flux within the 35.8 km<sup>2</sup> upscaling area  
470 was 0.05 mmol m<sup>-2</sup> h<sup>-1</sup>, which is close to 0.04 mmol m<sup>-2</sup> h<sup>-1</sup> obtained by Tuovinen et al. (2019), who  
471 combined EC data with footprint modeling to statistically determine LCT group-specific CH<sub>4</sub>  
472 fluxes. Within this upscaling area, we estimate that 28 % of the area emitted CH<sub>4</sub>, while the other  
473 habitats either consumed atmospheric CH<sub>4</sub> (barren and lichen tundra, dwarf-shrub tundra, meadow)  
474 or were close to neutral relative to the atmosphere (Fig. 4, Table 3). The relationship between

475 vascular plant LAI and CH<sub>4</sub> flux was confused by the occurrence of large CH<sub>4</sub> fluxes in plots with  
476 little or no vegetation. Those cases occurred at the wettest fen plot and bare-peat and vehicle track  
477 plots (Figs. 3–5). High LAI, high WT and high CH<sub>4</sub> emissions systematically co-occurred in wet  
478 fen (Fig. 6). The eroded bare-peat surface of dry fen and the disturbed vehicle tracks had high CH<sub>4</sub>  
479 emissions, where erosion or disturbance may have created CH<sub>4</sub> flux hotspots due co-occurrence of  
480 permafrost scars, water saturation, and recently thawed organic matter (*e.g.*, Bubier et al. 1995,  
481 McCalley et al. 2014, Wickland et al. 2020). These are small-scale landscape features, while in a  
482 larger scale, our data encourage applying indices of wetness and vegetation as a means of CH<sub>4</sub> flux  
483 upscaling in a tundra environment.

484 The recognition of CH<sub>4</sub> consuming tundra habitats is important for accurately estimating  
485 the net CH<sub>4</sub> balance of tundra. The substantial uptake of atmospheric CH<sub>4</sub> by lichen tundra (here a  
486 mixture of bare ground and sparse vegetation) in Tiksi was inferred by Tuovinen et al. (2019) based  
487 on a source allocation analysis of EC data: the average flux of the consuming area was estimated at  
488 -0.03 mmol m<sup>-2</sup> h<sup>-1</sup>, which corresponded to -22 % of the total upscaled CH<sub>4</sub> flux. In this study, the  
489 average seasonal CH<sub>4</sub> uptake was -0.02 mmol m<sup>-2</sup> h<sup>-1</sup> in the barren tundra and an order of magnitude  
490 lower in meadow, dwarf-shrub tundra,. Our upscaling exercise suggested a CH<sub>4</sub> sink that  
491 corresponded -9 % of the regional CH<sub>4</sub> balance. This difference may originate from the LCT-  
492 weighting and the small sample of the chamber-based estimate and, in general, demonstrates the  
493 inherent sensitivity involved in upscaling of fluxes of opposite direction.

494 High consumption of atmospheric CH<sub>4</sub> in barrens is associated with the high affinity  
495 methanotrophs (Emmerton et al. 2014, Jørgensen et al. 2014, D’Imperio et al. 2017, St Pierre et al.  
496 2019). In our summary of CH<sub>4</sub> fluxes in mineral-rich dry tundra (Table 4), the consumption values  
497 of this study and Tuovinen et al. (2019) are the highest, but similar rates have been observed in  
498 other dry tundra sites with little or no vegetation. For instance, on Disko Island, Greenland, which  
499 consists of similar land cover types to Tiksi, uptake of CH<sub>4</sub> by bare ground was -0.005–0.01 mmol

500  $\text{m}^{-2} \text{h}^{-1}$  during the growing season, while a mean flux of  $-0.003\text{--}0.004 \text{ mmol m}^{-2} \text{h}^{-1}$  was observed  
 501 in dry tundra heath (D'Imperio et al. 2017). These consumption rates associated with tundra barrens  
 502 and high-affinity methanotrophs can be even higher than those measured on north-boreal forest  
 503 soils (for instance,  $-0.01 \text{ mmol m}^{-2} \text{h}^{-1}$ , Lohila et al. 2016).

504

505 Table 4. Summary of reported consumption rates of atmospheric  $\text{CH}_4$  in mineralsoil dry tundra.

Location	Habitat type	Mean ( $\mu\text{mol m}^{-2} \text{h}^{-1}$ )	Min	Max	Reference
Narsarsuaq, Greenland	low elevation heath vegetation	-1.2	-4.0	-0.2	St Pierre et al. 2019
Narsarsuaq, Greenland	high elevation heath vegetation	-2.6	-11.9	3.6	St Pierre et al. 2019
Disko Island, Greenland	low elevation heath vegetation	-3.8	-12.1	-1.1	St Pierre et al. 2019
Disko Island, Greenland	high elevation heath vegetation	-3.5	-12.1	-1.3	St Pierre et al. 2019
Tierra del Fuego, Argentina	alpine tundra	0.5	-16.6	10.3	Sá et al. 2019
Disko Island, Greenland	dry tundra heath <sup>1</sup>	-4.0	-4.4	-2.5	D'Imperio et al. 2017
Disko Island, Greenland	bare ground <sup>1</sup>	-9.0	-15.0	-3.8	D'Imperio et al. 2017
Disko Island, Greenland	Betula nana and Salix sp. heath	-4.0			Christiansen et al. 2014
Axel Heiberg Island, CA	vegetated ice-wedge polygon		-2.7	-0.3	Lau et al. 2015
Lake Hazen, Ellesmere I., CA	polar desert <sup>2</sup>	-3.6	-7.0	0.0	Emmerton et al. 2014
Zackenberg Valley, Greenland	moist tundra	-3.1	-7.0	-2.0	Jørgensen et al. 2014
Zackenberg Valley, Greenland	dry tundra & barren ground	-7.0	-16.0	-4.0	Jørgensen et al. 2015
Zackenberg Valley, Greenland	tundra heath	-1.3	-6.0	0.0	Christensen et al. 2000
Okse Bay, Ellesmere I., CA	polar desert <sup>3</sup>	-0.5			Brummel et al. 2014
Petterson R., Ellesmere I., CA	polar desert <sup>3</sup>	-0.04			Brummel et al. 2014
Dome, Ellesmere I., CA	polar desert <sup>3</sup>	-0.5			Brummel et al. 2014
BAWLD- $\text{CH}_4$ Synthesis	dry tundra		-2.9	5.2	Kuhn et al. 2021
BAWLD- $\text{CH}_4$ Synthesis	boreal forest		-2.6	-0.5	Kuhn et al. 2021
Tiksi, RU	Barren & lichen tundra <sup>4</sup>	-29			Tuovinen et al. 2019
Tiksi, RU	lichen tundra mean	-11.3	-57.9	-0.4	This study
Tiksi, RU	barren	-18.1	-57.9	-3.0	This study
Tiksi, RU	vegetated	-6.0	-34.7	-0.4	This study
Tiksi, RU	meadow	-1.0	-21.1	24.5	This study
Tiksi, RU	dwarf-shrub tundra	-0.2	-2.9	20.3	This study
Tiksi, RU	bog	-2.1	-14.8	6.6	This study

506 <sup>1)</sup> mean estimated from a figure, <sup>2)</sup> min and max estimated from a figure, <sup>3)</sup> one-three day  
 507 measurement, <sup>4)</sup> estimated from EC measurements with a statistical model.

508

509 **5 Conclusions**

510 Our results provide new observations of carbon exchange for the prostrate dwarf shrub tundra sub-  
511 zone, which covers a substantial area of the Arctic. These data augment the knowledge on the  
512 functional diversity, namely the distribution of different land-cover types and their emission factors,  
513 across the vast arctic tundra and will lend support to bottom-up and top-down extrapolations across  
514 the Arctic. Graminoid vegetation that favored the wet and moist habitats, such as wet fens, was  
515 characterized by large CO<sub>2</sub> uptake and CH<sub>4</sub> emissions. In addition, our data support the observation  
516 of notable consumption of atmospheric CH<sub>4</sub> in barren tundra that has substantial coverage across  
517 the Arctic. The heterogeneity of landscape and the related large spatial variability of CO<sub>2</sub> and CH<sub>4</sub>  
518 fluxes observed in this study encourage to monitor the Arctic sites for changes in habitat type  
519 distribution. Such changes can include the forming of meadows and wet fens and appearance of  
520 new vegetation communities, such as erect shrubs, that benefit of warming-induced changes in thaw  
521 depth and soil wetness. The spatial extrapolation based on a small number of measurement points  
522 involves inherent uncertainty but still allowed us to identify key relationships between CO<sub>2</sub> and  
523 CH<sub>4</sub> fluxes and vegetation and moisture features, which can be utilized in more robust upscaling  
524 studies that make use of EC measurements.

525

526 *Data availability.* The flux data used in this study can be accessed via the Zenodo data repository:  
527 Juutinen, Sari. (2022). Dataset for a manuscript entitled Variation in CO<sub>2</sub> and CH<sub>4</sub> Fluxes Among  
528 Land Cover Types in Heterogeneous Arctic Tundra in Northeastern Siberia [Data set]. Zenodo.  
529 <https://doi.org/10.5281/zenodo.5825705>

530

531 *Author contributions*

532 TL, MA, and SJ designed the study. TL, MA, and AM took care of the overall site governance and  
533 maintenance. VI, ML, TL, JM, JN, EV, TL, TV, and MA conceived the field measurements of CO<sub>2</sub>  
534 and CH<sub>4</sub>, vegetation, and environmental variables. In addition, ML calculated green chromatic

535 coordinates, and MA and J-PT postprocessed the EC data and J-PT modeled the footprint and  
536 estimated footprint LCT fractions. AR and TV processed and modelled the landcover data and  
537 estimated TWI and NDVI for the plots and area. SJ compiled the chamber flux data and conducted  
538 the data analyses and spatial extrapolations and wrote the manuscript with contributions from all co-  
539 authors.

540

541 *Competing interests*

542 The authors declare that they have no conflict of interest.

543

544 *Acknowledgements*

545 We thank G. Chumachenko, O. Dmitrieva, and E. Volkov at the Tiksi Observatory and the  
546 Yakutian Hydrometeorological Service for their kind assistance in carrying out and organizing the  
547 field campaigns and Lauri Rosenius for assistance in the field work. This study was financially  
548 supported by the Academy of Finland, projects “Greenhouse gas, aerosol and albedo variations in  
549 the changing Arctic” (project no. 269095), “Carbon balance under changing processes of Arctic and  
550 subarctic cryosphere” (project no. 285630), “Constraining uncertainties in the permafrost-climate  
551 feedback” (project no. 291736) and “Carbon dynamics across Arctic landscape gradients: past,  
552 present and future” (project no. 296888); the European Commission, FP7 project “Changing  
553 permafrost in the Arctic and its global effects in the 21st century (PAGE21, project no. 282700)”;  
554 and the Nordic Council of Ministers, DEFROST Nordic Centre of Excellence within NordForsk.

555

556 **References**

557 AARI: Archive of Tiksi standard meteorological observations (1932–2016), Russian Federal  
558 Service for Hydrometeorology and Environmental Monitoring, St Petersburg, Russia,

559 available at: [http://www.aari.ru/resources/d0024/archive/description\\_e.html](http://www.aari.ru/resources/d0024/archive/description_e.html), last  
560 access: 13 September 2018.

561 Aurela, M., Laurila, T., and Tuovinen, J-P.: The timing of snow melt controls the annual CO<sub>2</sub>  
562 balance in a subarctic fen, *Geophysical Research Letters* 31, L16119,  
563 doi:10.1029/2004GL020315, 2004.

564 Brummel, M.E., Farrell, R.E., Hardy, S.P., and Siciliano, S.D., Greenhouse gas production and  
565 consumption in High Arctic deserts, *Soil Biology and Biochemistry*, 68, 158–165,  
566 <https://doi.org/10.1016/j.soilbio.2013.09.034>, 2014.

567 Bartlett, K. B., and Harriss, R. C., Review and assessment of methane emissions from wetlands.  
568 *Chemosphere*, 26, 261–320, 1993.

569 Bubier, J.L., Moore, T.R., Bellisario, L., Comer, N.T., and Crill, P.M: Ecological controls on  
570 methane emissions from a northern peatland complex in the zone of discontinuous  
571 permafrost, Manitoba, Canada. *Global Biogeochemical Cycles* 9. 455–470, 1995.

572 Callaghan, T.V., Johansson, M., Brown, R.D. et al. Multiple Effects of Changes in Arctic Snow  
573 Cover, 2011, *AMBIO* 40, 32–45 (2011). <https://doi.org/10.1007/s13280-011-0213-x>

574 Chen, L., Aalto, J., and Luoto, M.: Significant shallow–depth soil warming over Russia during the  
575 past 40 years. *Global and Planetary Change*, 197, 103394,  
576 doi.org/10.1016/j.gloplacha.2020.103394, 2021.

577 Christensen, T. R., Friberg, T., Sommerkorn, M., Kaplan, J., Illeris, L., Soegaard, H., Nordstroem,  
578 C., and Jonasson, S., Trace gas exchange in a high-Arctic valley: 1. Variations in CO<sub>2</sub>  
579 and CH<sub>4</sub> Flux between tundra vegetation types, *Global Biogeochemical Cycles*, 14,  
580 701– 713, doi:10.1029/1999GB001134, 2000.

581 Christiansen, J.R., Romero, A.J.B., Jørgensen, N.O.G., Glaring, M.A., Jørgensen, C.J., Berg, L.K.,  
582 Elberling, B. Methane fluxes and the functional groups of methanotrophs and

583 methanogens in a young Arctic landscape on Disko Island, West Greenland,  
584 Biogeochemistry, 122, 15–33, 2014.

585 D'Imperio, L., Skov Nielsen, C., Westergaard-Nielsen, A., Michelsen, A., and Elberling, B.:  
586 Methane oxidation in contrasting soil types: responses to experimental warming with  
587 implication for landscapeintegrated CH<sub>4</sub> budget. Global Change Biology 23, 966–  
588 976, doi: 10.1111/gcb.13400, 2017.

589 Eckhardt, T., Knoblauch, C., Kutzbach, L., Holl, D., Simpson, G., Abakumov, E., and Pfeiffer, E-  
590 M.: Partitioning net ecosystem exchange of CO<sub>2</sub> on the pedon scale in the Lena River  
591 Delta, Siberia. Biogeosciences 16, 1543–1562, doi:10.5194/bg-16-1543-2019, 2019.

592 Emmerton, C.A., St Louis, V.L., Lehnher, I., Humphreys, E.R., Rydz, E., Kosolofski, H.R. The net  
593 exchange of methane with high Arctic landscapes during the summer growing season.  
594 Biogeosciences, 11, 3095–3106, 2014.

595 Euskirchen, E.S., Bret-Harte, M.S., Shaver, G.R., Edgar, C.W., and Romanovsky, V.E.: Long-Term  
596 Release of Carbon Dioxide from Arctic Tundra Ecosystems in Alaska. Ecosystems 20,  
597 960–974, doi: 10.1007/s10021-016-0085-9, 2017.

598 Gorelick, N., Hancher, M., Dixon, M., Ilyushchenko, S., Thau, D., and Moore, R.: Google Earth  
599 Engine: Planetary-scale geospatial analysis for everyone. Remote Sensing of  
600 Environment, 202, 18-27, doi.org/10.1016/j.rse.2017.06.031, 2017.

601 Hashemi, J., Zona, D., Arndt, K.A., Kalhori, A., and Oechel, W.C.: Seasonality buffers carbon  
602 budget variability across heterogeneous landscapes in Alaskan Arctic Tundra.  
603 Environ. Res. Lett. in press <https://doi.org/10.1088/1748-9326/abe2d1>, 2021.

604 Humphreys, E.R. and Lafleur, P.M.: Does earlier snowmelt lead to greater CO<sub>2</sub> sequestration in  
605 two low Arctic tundra ecosystems? Geophysical Research Letters 38, L09703,  
606 doi:10.1029/2011GL047339, 2011.

607 IPCC Summary for Policymakers in Climate Change 2013: The Physical Science Basis (eds  
608 Stocker, T. F. et al.) 3–29, Cambridge Univ, Press, 2013.

609 Jørgensen, C.J., Lund Johansen, K.M., Westergaard-Nielsen, A., and Elberling, B.: Net regional  
610 methane sink in High Arctic soils of northeast Greenland. *Nature Geoscience* 8, doi:  
611 10.1038/NGEO2305, 2014.

612 Juutinen, S., Virtanen, T., Kondratyev, V., Laurila, T., Linkosalmi, M., Mikola, J., Nyman, J.,  
613 Räsänen, A., Tuovinen, J-P., and Aurela, M.: Spatial variation and seasonal dynamics  
614 of leaf-area index in the arctic tundra – implications for linking ground observations  
615 and satellite images. *Environmental Research Letters* 12, doi.org/10.1088/1748-  
616 9326/aa7f85, 2017.

617 Kuhn, M. A., Varner, R. K., Bastviken, D., Crill, P., MacIntyre, S., Turetsky, M., Walter Anthony,  
618 K., McGuire, A. D., and Olefeldt, D.: BAWLD-CH<sub>4</sub>: a comprehensive dataset of  
619 methane fluxes from boreal and arctic ecosystems, *Earth Syst. Sci. Data*, 13, 5151–  
620 5189, <https://doi.org/10.5194/essd-13-5151-2021>, 2021.

621 Lau, M.C.Y., Stackhouse, B.T., Layton, A.C., Chauhan, A., Vishnivetskaya, T.A., Chourey, K.,  
622 Ronholm, J., Mykytczuk, N.C.S., Bennett, P.C., Lamarche-Gagnon, G., Burton, N.,  
623 Pollard, W.H., Omelon, C.R., Medvigy, D.M., Hettich, R.L., Pfiffner, S.M., Whyte,  
624 L.G., and Onstott, T.C.: An active atmospheric methane sink in high Arctic mineral  
625 cryosols. *The ISME Journal* 9, 1880–1891, doi:10.1038/ismej.2015.13, 2015.

626 Lafleur, P.M., Humphreys, E.R., St. Louis, V.L., Myklebust, M.C., Papakyriakou, T., Poissant, L.,  
627 Barker, J.D., Pilote, M., and Swystun, K.A.: Variation in Peak Growing Season Net  
628 Ecosystem Production Across the Canadian Arctic. *Environmental Science and  
629 Technology* 46, 7971–7977, doi.org/10.1021/es300500m, 2012.

630 Lara, M.J., McGuires, A.D., Euskirchen, E.S., Genet H., Yi, S., Rutter, R., Iversen, C., Sloan, V.,  
631 and Wullschleger, S.D.: Local-scale Arctic tundra heterogeneity affects regional-scale

632 carbon dynamics- *Nature Communications* 11, 4925, doi:10.1038/s41467-020-18768-  
633 z, 2020.

634 Lohila, A., Aalto, T., Aurela, M., Hatakka, J., Tuovinen, J-P., Kilkki, J., Penttilä, T., Vuorenmaa, J.,  
635 Hänninen, P., Sutinen, R., Viisanen, Y., and Laurila, T.: Large contribution of boreal  
636 upland forest soils to a catchment-scale CH<sub>4</sub> balance in a wet year. *Geophysical*  
637 *Research Letters* 43, 2946–2953, doi.org/10.1002/2016GL067718, 2016.

638 Marushchak, M.E., Kiepe, I., Biasi, C., Elsakov, V., Friberg, T., Johansson, T., Soegaard, H.,  
639 Virtanen, T., and Martikainen, P.J.: Carbon dioxide balance of subarctic tundra from  
640 plot to regional scales. *Biogeosciences* 10, 437–452, doi:10.5194/bg-10-437-2013,  
641 2013.

642 McCalley, C.K., Woodcroft, B.J., Hodgkins, S.B., Wehr, R.A., Kim, E-H., Mondav, R., Crill, P.M.,  
643 Chanton, J.P., Rich, V.I., Tyson, G.W., and Saleska, S.R.: Methane dynamics  
644 regulated by microbial community response to permafrost thaw. *Nature* 514, 478–451,  
645 doi:10.1038/nature13798, 2014.

646 McFadden, J.P., Eugster, W., and Chapin, F.S., III: A regional study of the controls on water vapor  
647 and CO<sub>2</sub> exchange in arctic tundra. *Ecology* 84, 2762–2776, doi:10.1890/01-0444,  
648 2003.

649 McGuire, A. D., Christensen, T. R., Hayes, D., Heroult, A., Euskirchen, E., Kimball, J. S., Koven,  
650 C., Lafleur, P., Miller, P. A., Oechel, W., Peylin, P., Williams, M., and Yi, Y.: An  
651 assessment of the carbon balance of Arctic tundra: comparisons among observations,  
652 process models, and atmospheric inversions, *Biogeosciences*, 9, 3185–3204,  
653 <https://doi.org/10.5194/bg-9-3185-2012>, 2012.

654 McGuire, A.D., Lawrence, D.M., Koven, C., Clein, J.C., Burke, E., Chen, G., Jafarov, E.,  
655 MacDougall, A.H., Marchenko, S., Nicolsky, D., Peng, S., Rinke, A., Ciais, P.,  
656 Gouttevin, I., Hayes, D.J., Jin, D., Krinner, G., Moore, J.C., Romanovsky, V.,

657 Schädel, C., Schaefer, K., Schuur, E.A.G., and Zhuang, Q.: Dependence of the  
658 evolution of carbon dynamics in the northern permafrost region on the trajectory of  
659 climate change, PNAS 115,: 3882–3887, doi/10.1073/pnas.1719903115, 2018.

660 Mikola, J., Virtanen, T., Linkosalmi, M., Vähä, E., Nyman, J., Postanogova, O., Räsänen, A.,  
661 Kotze, D.J., Laurila, T., Juutinen, S., Kondratyev, V., and Aurela, M.: Spatial  
662 variation and linkages of soil and vegetation in the Siberian Arctic tundra – coupling  
663 field observations with remote sensing data. Biogeosciences 15, 2781–2801, 2018.

664 Oh, Y., Zhuang, Q., Liu, L., Welp, L.R., Lau, M.C.Y., Onstott, T.C., Medvigy, D., Bruhwiler, L.,  
665 Dlugokencky, E.J., Hugelius, G., D'Imperio, L., and Elberling, B. Reduced net  
666 methane emissions due to microbial methane oxidation in a warmer Arctic. Nature  
667 Climate Change 10, 317–321, 2020.

668 St Pierre, K.A., Kortegaard Danielsen, B., Hermesdorf, L., D'Imperio, L., Lønsmann Iversen, L.,  
669 Elberling, B.: Drivers of net methane uptake across Greenlandic dry heath tundra  
670 landscapes. Soil Biology and Biochemistry 138: 107605,  
671 doi.org/10.1016/j.soilbio.2019.107605, 2019.

672 Räsänen, A., Manninen, T., Korkiakoski, M., Lohila, A., and Virtanen, T.: Predicting catchment-  
673 scale methane fluxes with multi-source remote sensing. Landscape Ecology 36, 1177–  
674 1195. <https://doi.org/10.1007/s10980-021-01194-x>. 2021.

675 Richardson, A.D.: Tracking seasonal rhythms of plants in diverse ecosystems with digital camera  
676 imagery. New Phytologist 222, 1742–1750, doi: 10.1111/nph.15591, 2019.

677 Sá, M.M.F., Schaefer, C.E.G.R., Loureiro, D.C., Simas, F.N.B., Alves, B.J.R., de Sá Mendonça, E.,  
678 Barreto de Figueiredo, E., La Scala, N., Panosso, A.R., Fluxes of CO<sub>2</sub>, CH<sub>4</sub>, and  
679 N<sub>2</sub>O in tundra-covered and Nothofagus forest soils in the Argentinian Patagonia,  
680 Science of The Total Environment, 659, 401-409,  
681 <https://doi.org/10.1016/j.scitotenv.2018.12.328>, 2019.

682 Saunois, M., Stavert, A.R., Poulter, B., Bousquet, P., Canadell, J.G., Jackson, R.B., Raymond, P.A.,  
683 Drugokencky, E.J., Houweling, S., Patra, P.K. and Ciais, P.: The global methane  
684 budget 2000–2017. *Earth System Science Data*, 12, 1561–1623, 2020.

685 Shaver, G.R., Street, L.E., Rastetter, E.B., van Wijk, M.T., and Williams, M.: Functional  
686 convergence in regulation of net CO<sub>2</sub> flux in heterogeneous tundra landscapes in  
687 Alaska and Sweden. *Journal of Ecology* 95, 802–817, 2007.

688 Street, L.E., Shaver, G.R., Williams, M., and van Wijk, M.T.: What is the relationship between  
689 changes in canopy leaf area and changes in photosynthetic CO<sub>2</sub> flux in arctic  
690 ecosystems? *Journal of Ecology* 95, 139–150, 2007.

691 Ter Braak, C.J.F. and Šmilauer, P.: Canoco reference manual and user's guide: software for  
692 ordination (version 5.0). Microcomputer Power, Ithaca, NY, USA, 2012.

693 Treat, C.C., Marushchak, M.E., Voigt, C., Zhang, Y., Tan, Z., Zhuang, Q., Virtanen, T.A., Räsänen,  
694 A., Biasi, C., Hugelius, G., Kaverin, D., Miller, P.A., Stendel, M., Romanovsky, V.,  
695 Rivkin, F., Martikainen, P.J., and Shurpali, N.J. Tundra landscape heterogeneity, not  
696 interannual variability, controls the decadal regional carbon balance in the Western  
697 Russian Arctic. *Global Change Biology* 24, 5188–5204, doi: 10.1111/gcb.14421,  
698 2018.

699 Tuovinen, J-P., Aurela, M., Hatakka, J., Räsänen, A., Virtanen, T., Mikola, J., Ivakhov, V.,  
700 Kondratyev, V., and Laurila, T.: Interpreting eddy covariance data from  
701 heterogeneous Siberian tundra: land-cover-specific methane fluxes and spatial  
702 representativeness. *Biogeosciences* 16, 255–274, doi.org/10.5194/bg-16-255-2019,  
703 2019.

704 Uttal, T., Starkweather, S., Drummond, J. R., Vihma, T., Makshtas, A. P., Darby, L. S., Burkhart,  
705 J. F., Cox, C. J., Schmeisser, L. N., Haiden, T., Maturilli, M., Shupe, M. D., de Boer,  
706 G., Saha, A., Grachev, A. A., Crepinsek, S. M., Bruhwiler, L., Goodison, B.,

McArthur, B., Walden, V. P., Dlugokencky, E. J., Persson, P. O. G., Lesins, G., Laurila, T., Ogren, J. A., Stone, R., Long, C. N., Sharma, S., Massling, A., Turner, D. D., Stanitski, D. M., Asmi, E., Aurela, M., Skov, H., Eleftheriadis, K., Virkkula, A., Platt, A., Førland, E. J., Iijima, Y., Nielsen, I. E., Bergin, M. H., Candlish, L., Zimov, N. S., Zimov, S. A., O'Neill, N. T., Fogal, P. F., Kivi, R., Konopleva-Akish, E. A., Verlinde, J., Kustov, V.Y., Vasel, B., Ivakhov, V.M., Viisanen, Y., and Intrieri, J. M.: International Arctic Systems for Observing the Atmosphere: An International Polar Year Legacy Consortium. *Bull. Am. Meteor. Soc.*, 97, 1033–1056. doi:10.1175/BAMS-D-14-00145.1, 2016.

Schuur, E.A.G., Natali, S.M., Oken, K.L., Bracho, R., Krapek, J.P., Risk, D., and Nickerson, N.R.: Increased wintertime CO<sub>2</sub> loss as a result of sustained tundra warming, *Journal of Geophysical Research Biogeosciences* 121, 249–265, doi:10.1002/2014JG002795, 2016.

., P., Jorgenson, M.T., Koch, J.C., Kanevskiy, M., and Striegl, R.G.: Carbon dioxide and methane flux in a dynamic Arctic tundra landscape: Decadal-scale impacts of ice wedge degradation and stabilization. *Geophysical Research Letters*, 47, e2020GL089894, doi:10.1029/2020GL089894, 2020.

en, M.K., van Huissteden, J., Parmentier, F.J.W., Petrescu, A.M.R., Dolman, A.J., Maximov, T.C., Kononov, A.V., Karsanaev, S.V., and Suzdalov, D.A.: The growing season greenhouse gas balance of a continental tundra site in the Indigirka lowlands, NE Siberia. *Biogeosciences* 4, 985–1003, doi.org/10.5194/bg-4-985-2007, 2007.

-M., Virtanen, T., Lehtonen, A., Rinne, J., and Luoto, M.: The current state of CO<sub>2</sub> flux chamber studies in the Arctic tundra: A review. *Progress in Physical Geography*, 42, 162–184, 2018.

731 Virkkala, et al.: Statistical upscaling of ecosystem CO<sub>2</sub> fluxes across the terrestrial tundra and  
732 boreal domain: regional patterns and uncertainties. *Global Change Biology*,  
733 doi:10.1111/GCB.15659, 2021.

734 Virtanen, T. and Ek, M.: The fragmented nature of tundra landscape. *International Journal of  
735 Applied Earth Observation and Geoinformation* 27, 4–12, 2014.

736 Zhang, W., Jansson, P-E., Sigsgaard, C., McConnell, A., Manon Jammet, M., Westergaard-Nielsen,  
737 A., Lund, M., Friberg, T., Michelsen, A., and Elberling, B.: Model-data fusion to  
738 assess year-round CO<sub>2</sub> fluxes for an arctic heath ecosystem in West Greenland  
739 (69°N). *Agricultural and Forest Meteorology* 272–273, 176–186, 2019.

740

741

742

743

744

745

746

747

748

749

750

751

752

753

754

755

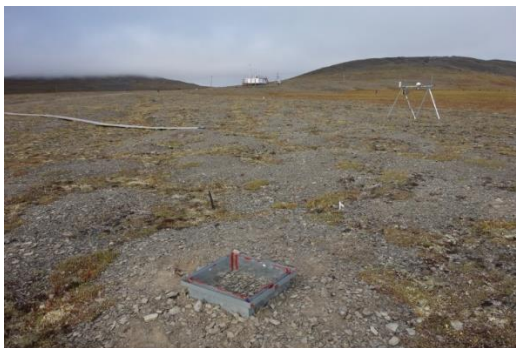
756

757

758

759

760 **Appendix A**



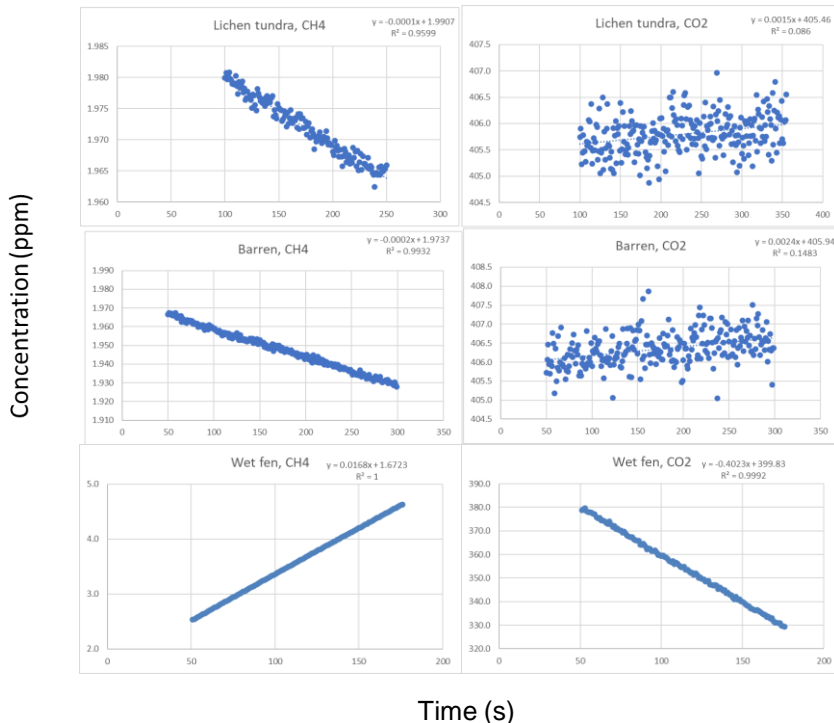
761

762 Fig. A1. Examples of the barren (left) and lichen tundra (right) plots with close views (bottom).  
763 Vegetation consists of lichens *Flavocetraria* sp., *Thamnolia* sp., *Alectoria* sp., dwarf-shrubs *Dryas*  
764 *octopetala*, *Vaccinium vitis-idaea*, *Cassiope tetragona*, and graminoids and forbs such as *Carex*  
765 *spp.* and *Polygonum viviparum*.

766

767

768

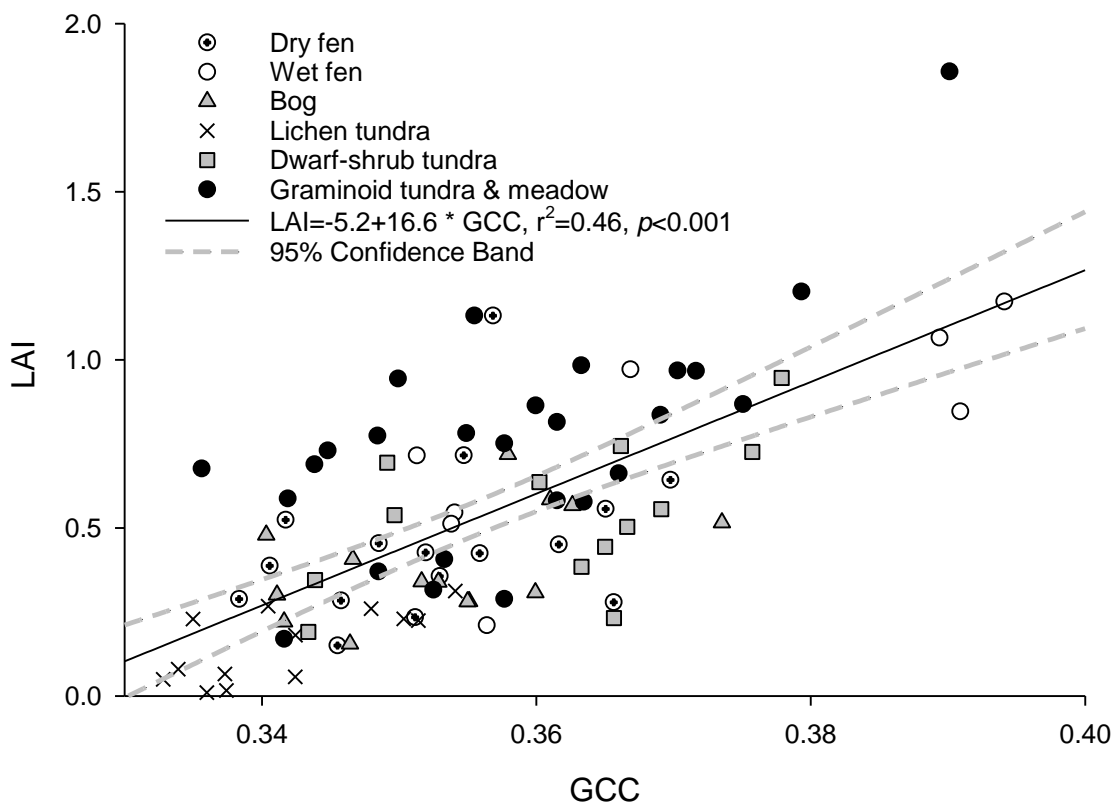


769

770 Fig. A2. Examples of gas concentrations in chambers measured using the LRG analyzer (DLT-100,  
 771 Los Gatos Research, Inc., San Jose, CA, USA). The examples represent lichen tundra, barren, and  
 772 wet fen.

773

774



775

776 Fig. A3. Relationship between GCC and vascular plant LAI in the harvested plots. LCTs are  
 777 indicated with symbols. In the LCT-specific regressions (not shown), the coefficient of  
 778 determination ( $R^2_{adj.}$ ) was lowest for dry fen (0.06) and highest for wet fen (0.54). Regression  
 779 slopes varied from 8.3 for dry fen to 17.8 for the combined graminoid tundra and meadow LCT.

780